ADVANCED FUNCTIONAL MATERIALS
www.afm-journal.de

Six-Inch High-Purity Lead Halide Perovskite Wafer Derived from Ceramic Manufacturing Technique

Shilin Liu, Yijing Ding, Yuwei Li, Wenzhe Rong, Yi Xu, Xianyu Zhao, Jixi Zhou, Tengwu Wang, Damian Chinedu Onwudiwe, Byung Seong Bae, Mehmet Ertuğrul, Ying Zhu, Wei Lei, Qing Li,* and Xiaobao Xu**

Lead halide perovskites exhibit exceptional optoelectronic properties but face industrialization barriers due to the inability to fabricate large-area, high-quality wafers. Inspired by ceramic manufacturing techniques, a 6-inch high-purity perovskite wafer is developed, achieving carrier mobility, lifetime, and defect concentrations comparable to single crystals. This method demonstrates universality across diverse perovskites and enables heterojunction wafers, marking significant progress in carrier dynamics control. As a result, an X-ray sensing array with 256 × 256 pixels is constructed using a 10 × 10 cm^2 perovskite heterojunction wafer, which exhibits a sensitivity of 36532 μCGy_{air}^{-1} cm^{-2} and a low detection limit of 139 nGy_{air} s^{-1}, superior to those in a single-crystal detector (10640 μCGy_{air}^{-1} cm^{-2} and 247 nGy_{air} s^{-1}). This breakthrough establishes a scalable pathway to industrial-scale perovskite optoelectronics, overcoming critical manufacturing barriers while enabling high-performance radiation imaging systems through wafer-level heterostructure engineering.

1. Introduction

The unique combination of low-cost raw materials, facile synthesis, and tailored optical properties has propelled lead halide perovskites ($APbX_3$; A^+ = $CH_3NH_3^+$ [MA^+], $CH(NH_2)_2^+$ [FA^+], Cs+; X^- = I^-, Br^-, Cl^-) into diverse applications spanning solar cells,[1] direct X-ray/γ-ray detectors,[2] scintillators,[3] light-emitting diodes,[4] lasers,[5] nonlinear optics,[6] and visible/infrared photodetectors.[7] Despite these promising attributes, perovskite-based device development remains at the lab-scale stage, and industrial manufacturing still faces numerous difficulties.

Taking silicon-based devices as an example, they rely on standardized wafer-scale Si substrates (6–12-inch diameters) compatible with automated micro/nanofabrication workflows. However, the manufacture of perovskite wafers is still unsatisfactory. For example, melt-based techniques like Bridgman growth can produce all-inorganic variants (e.g., $CsPbX_3$),[8] but organic-inorganic hybrid perovskites suffer from thermal decomposition of volatile organic cations.[9] Similarly, solution-based crystallization methods, though versatile, exhibit poor reproducibility and scalability. Currently, state-of-the-art perovskite single crystals rarely exceed 5 cm in lateral dimensions and frequently contain structural inhomogeneities that compromise purity and optical quality.[9,10] These limitations bring a critical mismatch with the silicon-based device preparation technique. The absence of standardized perovskite wafer manufacturing hinders the compatibility with existing semiconductor foundry infrastructure—a prerequisite for transitioning from laboratory prototypes to commercial-scale production.

Recent advances in polycrystalline ceramic processing offer a promising pathway to fabricate large-area perovskite wafers. Lead halide perovskite wafers, synthesized via hot-pressing or sintering, have demonstrated X-ray detection sensitivities surpassing those of single-crystal $MAPbI_3$[11] and rivaling commercial CdTe detectors.[12] For instance, $Cs_3Bi_2I_3$ wafers[13] exhibit high carrier mobility and radiation hardness, while $Cs_2AgBiBr_6$[14] double perovskites achieve low dark currents and enhanced stability. However, existing ceramic fabrication methods yield opaque, mechanically fragile materials with limited thickness and poor

S. Liu, Y. Ding, Y. Li, W. Rong, Y. Xu, X. Zhao, J. Zhou, T. Wang, W. Lei, Q. Li, X. Xu
The Interdisciplinary Center
School of Electronic Science and Engineering
Southeast University
Nanjing 210000, China
E-mail: lw@seu.edu.cn; liqing@seu.edu.cn; xiaobaoxu@seu.edu.cn
S. Liu
Aviation Key Laboratory of Science Technology on Infrared Detector
Luoyang 471009, China
D. C. Onwudiwe
Department of Chemistry
School of Mathematics and Physical Sciences Faculty of Natural and Agricultural Sciences North-West University
Mafikeng Campus, Private Bag X2046, Mmabatho 2735, South Africa
B. S. Bae
Department of Electronics &Display Engineering
Hoseo University
Hoseo Ro 79, Asan, Chungnam 31499, Republic of Korea
M. Ertuğrul
Faculty of Engineering
Metallurgical and Materials Engineering
Karadeniz Technical University
Trabzon 61080, Turkey
Y. Zhu
E-xray Electronic Co. Ltd.
Suzhou 215131, China
The ORCID identification number(s) for the author(s) of this article can be found under https://doi.org/10.1002/adfm.202506879

DOI: 10.1002/adfm.202506879

optical transparency—properties directly linked to grain boundary defects, secondary phases, and porosity.[12a,15]

Taking transparency as an example, it requires dense, phase-pure microstructures with minimized light scattering—a hallmark of high-quality wafers. Transparent perovskite wafers can facilitate multifunctional applications including sensing arrays, nonlinear optics, rare-earth-doped lasers, and monolithic heterojunctions. Recent studies on lead-free variants like $(BA)_2CsAgBiBr_7$[16] and $(CH_3NH_3)_3BiI_9$[15d–f] highlight the growing interest in combining apparent transparency and optoelectronic performance. Nevertheless, no work has yet demonstrated freestanding, large-scale perovskite wafers (> 5 cm in diameter) with sub-millimeter thickness and visible/infrared transparency.

In this article, we demonstrate a high-purity, 6-inch, pinhole-free transparent perovskite wafer with ceramic manufacturing techniques. The high-quality perovskite wafers exhibit excellent optical and electrical properties, including defect levels, carrier mobility, and carrier lifetime comparable to those of single crystals. The multi-factor interaction mechanism of a precise control strategy within ceramic manufacturing techniques for improving the quality of perovskite wafers is revealed. The fabrication method can be expanded to different A-site cations and different halogen perovskites, as well as multilayer perovskite heterojunctions. Finally, an X-ray sensing array with 256 × 256 pixels was established on our perovskite heterojunction wafer with a high sensitivity of 36532 $\mu CGyair^{-1}\ cm^{-2}$ and a low detection limit of 139 $nGy_{air}\ s^{-1}$ superior to $MAPbBr_3$ single-crystal detector (10640 $\mu CGyair^{-1}\ cm^{-2}$ and 247 $nGy_{air}\ s^{-1}$). These results confirm the potential of our perovskite transparent wafer for constructing functional commercial devices using industrial manufacturing techniques.

2. Results and Discussion

In general, the high optical transparency of perovskite single crystals indicates their excellent properties, including phase-purity, crystallinity, defect, and optoelectronic behavior.[17] Opaqueness in polycrystalline materials mainly originates from optical anisotropy of grains, impurities or secondary phases at grain boundaries, high surface roughness ($\gg\lambda/10$), and pores.[18] Achieving high optical transparency in thick polycrystalline wafers requires stringent control of microstructural properties, including porosity, and crystal grain stacking. The schematic diagram in **Figure 1a** shows the difference in perovskite grain between the normal perovskite tablet with the hot-pressing technique and our proposed transparent perovskite wafer ($MAPbBr_3$). It is reasonable to believe that perovskite grain growth or grain boundary fusion is important to produce the pinhole-free perovskite wafer and ensure good transparency.

To achieve the transparent perovskite wafer, we employ a ceramic hot-pressing technique with a precise control strategy. In brief, we selected small perovskite single crystals from the solution process and fine-grind them to a micrometer scale. Subsequently, a perovskite wafer with a thickness of 0.6 mm can be fabricated via a ceramic fabrication method. Figure S1 (Supporting Information) illustrates this process. Figure S2 (Supporting Information) displays the influence of temperature, pressure, and time during hot-pressing on $MAPbBr_3$ wafers' transparency. Interestingly, $MAPbBr_3$ wafers change from opaque to transparent by adjusting the temperature, pressure, and time during the fabrication. With the accurate temperature of 150 °C and pressure of 200 MPa for 60 min, the obtained $MAPbBr_3$ wafer is transparent, which looks like a $MAPbBr_3$ single crystal. Figure 1b depicts the photograph of the ShunGui Laboratory Building (Southeast University) captured through a $MAPbBr_3$ transparent wafer, demonstrating the exceptional photon transmittance properties.

Surprisingly, the as-fabricated transparent $MAPbBr_3$ wafers can reach 6-inch wafer-grade. Table S1 (Supporting Information) summarizes the reported perovskite single crystals and polycrystalline tablets. To our best knowledge, our transparent $MAPbBr_3$ wafer is the largest and its size is significantly larger than that of perovskite single crystals. Figure 1c,d shows its optical image in the lab. Notably, one side is patterned with a gold electrode array. The gold electrode array is clearly visible on the reverse side. Figure 1e presents the optical transmission spectrum. Our $MAPbBr_3$ wafer exhibits a high optical transparency of ≈68% comparable to that of the single crystal (75%) within the 700–1100 nm range,[19] which is significantly higher than that in normal $MAPbBr_3$ tablets.

To verify that the transparency leads to excellent optoelectronic properties in the $MAPbBr_3$ wafer, we employed the time-of-flight technique to acquire the charge carrier drift time (τ_r) under different applied biases[20] (Figure S3, Supporting Information). The hole and electron mobility in $MAPbBr_3$ transparent wafer were calculated from the transit time and wafer thickness, yielding values of 99 and 180 $cm^2\ V^{-1}\ s^{-1}$, respectively (Figure 1f,g). The value is comparable to that of $MAPbBr_3$ single crystals (107 and 198 $cm^2\ V^{-1}\ s^{-1}$), which is significantly higher than that of normal $MAPbBr_3$ tablet (76 and 119 $cm^2\ V^{-1}\ s^{-1}$). This result indicates that our $MAPbBr_3$ transparent wafer manufacturing technique can efficiently eliminate the grain boundary and facilitate grain growth or fusion.

Quantification of wafer densities using the Archimedes method, as depicted in **Figure 2a** and Table S2 (Supporting Information), confirms a progressive increase in density with pressure up to 200 MPa, with the density approaching that of a $MAPbBr_3$ single crystal. However, when the pressure further goes up to 300 MPa, the density shows a clear decrease, which can be ascribed to the internal voids from wafer fragmentation. It should be noted that the time and temperature remain constant (150 °C and 60 min) throughout the process. If the time is shorter, incomplete compaction and fusion of $MAPbBr_3$ grains result in opacity at the wafer edges. Conversely, prolonging the time to 120 min leads to powder adherence to the mold, causing surface fracturing during demolding.

To verify the grain growth in our ceramic manufacture, we conducted a high-resolution X-ray rocking curve analysis of the (100) diffraction peak (Figure 2b; Figure S4, Supporting Information). According to the Scherrer formula, the grain size is inversely proportional to the full width at half maximum (FWHM). The results confirm that the wafer prepared at 150 °C exhibits larger grain sizes and better crystalline quality compared to those prepared at 50, 70, and 180 °C. Higher temperatures, such as 180 °C, induce the vaporization of the organic component MABr, leading to grain breakdown. To further accurately design the perovskite wafer manufacturing, Statistical Package for the Social Sciences software was used to generate the orthogonal table of temperature, pressure, and time. As shown in Tables S3 and S4

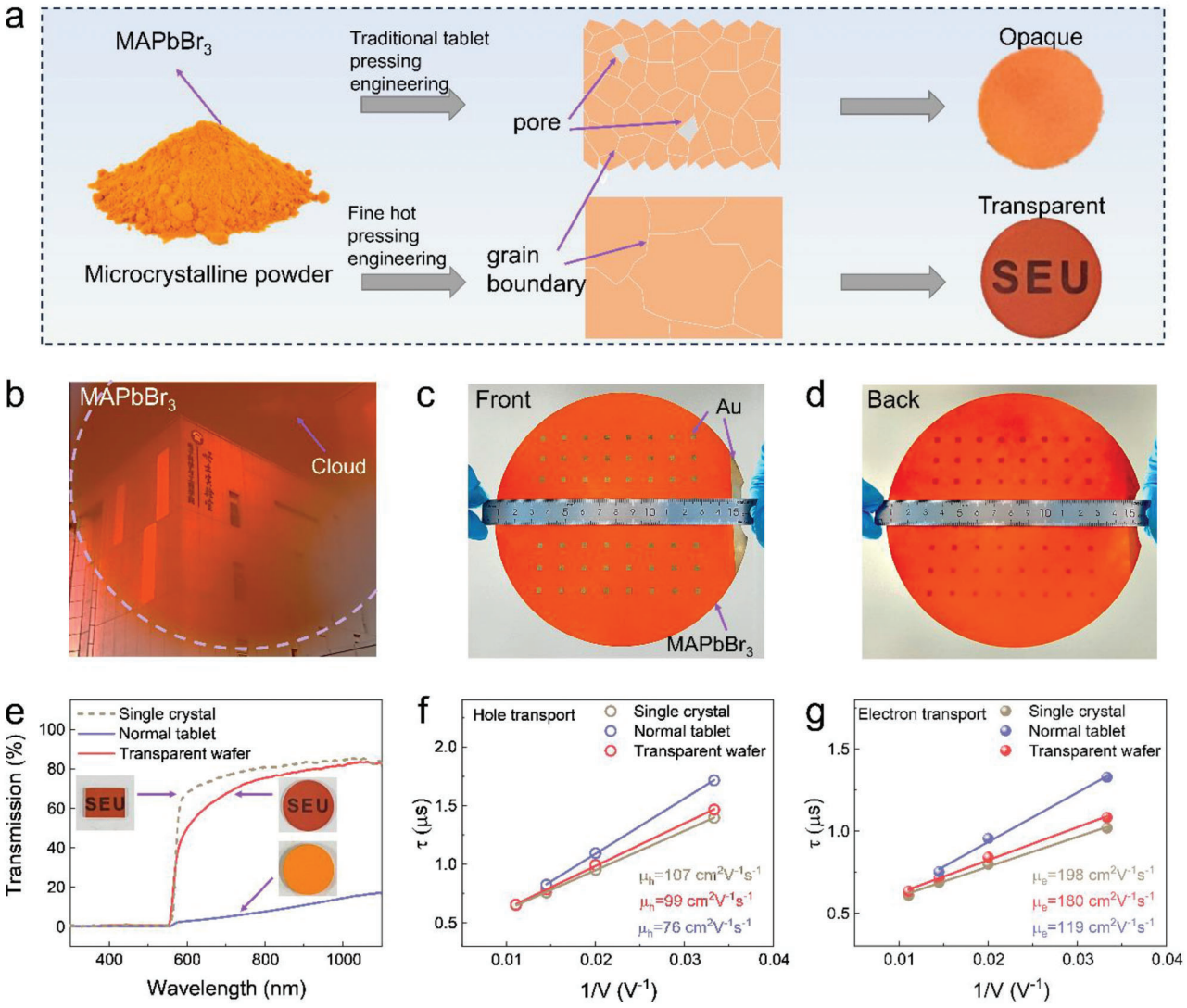

Figure 1. Six-inch transparent $MAPbBr_3$ wafers. a) The schematic illustration of the differences in grain boundary between the transparent wafer and the normal tablet. b) An image of the ShunGui Laboratory Building (Southeast University) captured through a $MAPbBr_3$ transparent wafer. c) Photograph of the 6-inch transparent wafer with gold electrode array on its front surface. d) Photograph of the 6-inch transparent wafer with the gold electrode array on the backside. e) The optical transmission spectrum. f) Hole and g) electron mobility.

(Supporting Information), the minimum K arithmetic mean values indicate the optimal settings are K_3 (150 °C), K_2 (200 MPa), and K_3 (60 min). Scanning electron microscopy images, as depicted in Figure S5 (Supporting Information), reveal that stress reduces the gaps between the grains, further confirming grain boundary fusion. Figure S6 (Supporting Information) depicts the dark *I*--*V* curves of Au/$MAPbBr_3$/Au devices. For each specific factor, the transparent $MAPbBr_3$ wafer prepared at 150 °C, 200 MPa, and 60 min exhibits the lowest dark current.

Figure 2c presents surface and cross-sectional Scanning electron microscope (SEM) images of single crystals and wafers with a thickness of ≈600 μm. The transparent wafer exhibits clear fused grain boundaries, demonstrating a continuous and compact surface morphology. In contrast, the normal tablet surface contains obvious pores. Cross-sectional SEM analysis further proves the compact density in the transparent wafer, as well as the single crystal. Figure 2d presents time-resolved photoluminescence (TRPL) spectra. The results demonstrate that the carrier lifetime of transparent $MAPbBr_3$ wafer significantly increases to 2.6 μs, which is quite longer than that of a normal tablet and approaches the value of 3.17 μs in a single crystal. As shown in Figure 2e, the $\mu\tau$ of $MAPbBr_3$ transparent wafer (1.8×10^{-4} cm^2 V^{-1}) is much higher than that of the normal tablet (4.3×10^{-5} cm^2 V^{-1}), comparable to that of single crystal (2.3×10^{-4} cm^2 V^{-1}).

Halide vacancies at grain boundaries generally act as ion migration channels in lead-based perovskites.[21] Temperature-dependent conductivity measurements were conducted to evaluate the electronic and ionic conductivity in transparent $MAPbBr_3$ wafers. The activation energy (E_a) of ion migration can be determined using the Nernst–Einstein relation:

$$\sigma\ (T) = \left(\frac{\sigma_0}{T}\right) \exp\left(-\frac{E_a}{Tk_B}\right) \quad (1)$$

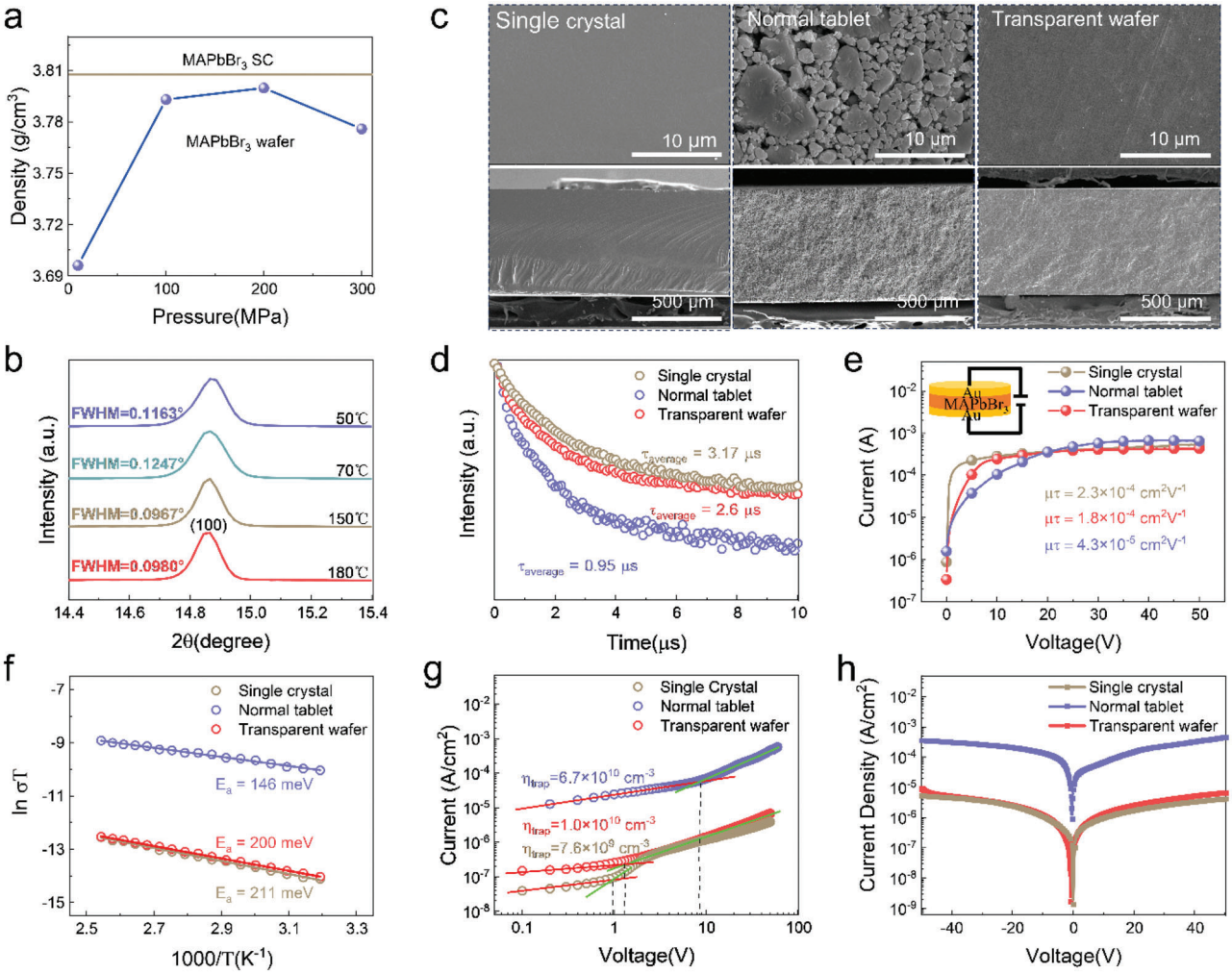

Figure 2. Characterization of the $MAPbBr_3$ transparent wafer. a) Density of $MAPbBr_3$ wafers prepared under different pressures. b) Magnified view of the (200) diffraction peak. c) SEM images of $MAPbBr_3$ single crystal and wafers. d) Time-resolved PL spectra. e) Bias-dependent photoconductivity. f) Temperature-dependent conductivity. g) SCLC curves of single crystals and wafers. h) *I–V* curve of Au/$MAPbBr_3$/Au devices based on single crystal and wafers under dark.

where σ_0 is a constant, T is the temperature, and k_B is the Boltzmann constant. As shown in Figure 2f, the E_a in transparent wafer (200 meV) is much higher than that of a normal tablet (146 meV), approaching the level of a single crystal (211 meV). It indicates the suppressed ion migration. As well, the dark current baseline was examined under a 30 V voltage for ≈7 min (Figure S7, Supporting Information) to extract the dark current drift D:[22]

$$D = \left| \left(J_t - J_0 \right) / tE \right| \tag{2}$$

where J_0 and J_t are the dark current densities at the beginning and end points, respectively, t is the duration time, and E is the electric field. The current baseline of a transparent wafer is much more stable with D of 5.6×10^{-4} nA cm^{-1} s^{-1} V^{-1}, which is three orders of magnitude lower than that of the normal tablet (1.73×10^{-1} nA cm^{-1} s^{-1} V^{-1}). The electronic noise spectral density in transparent wafers is much lower as illustrated in Figure S8 (Supporting Information). The trap density (n_{traps}) of the $MAPbBr_3$ wafers was investigated by the space-charge-limited current (SCLC) method. When the $MAPbBr_3$ wafer changes from opaque to transparent, the trap density decreases from 6.7×10^{10} to 1.0×10^{10} cm^{-3}, approaching the value of 7.6×10^9 for single crystals (Figure 2g). The diminished defect density and improved carrier mobility of the transparent wafer could be attributed to the substantially reduced porosity and grain boundary density. Figure 2h displays their *I–V* curve. It is inferred that ohmic contacts formed for transparent $MAPbBr_3$ wafers and single crystals. All the results confirm the optoelectronic properties in our transparent $MAPbBr_3$ wafer are comparable to those of single crystals.

To further identify the universality of our manufacturing technique, we apply it to various perovskites. Figure S9 (Supporting Information) shows photographs of as-fabricated perovskite transparent wafers with different A-site cations, B-site cation-doped perovskites, and different halogen perovskites. All the perovskite wafers display good optical transparency, indicating the advanced nature and universality of fine ceramic manufacturing engineering in the preparation of transparent perovskite wafers,

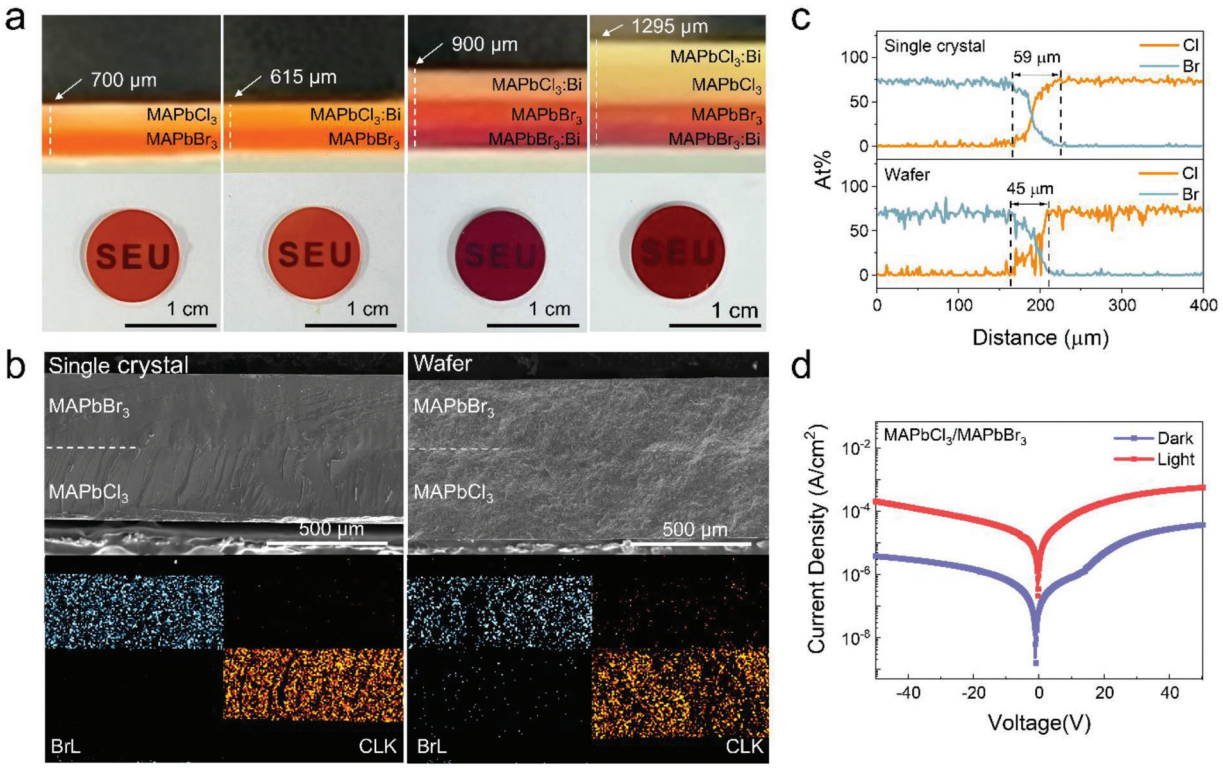

Figure 3. Characterization of the perovskite heterojunction wafers. a) Top optical and cross-sectional optical images of multilayer perovskite wafers. b) SEM images and EDS elemental mappings of $MAPbCl_3/MAPbBr_3$ single crystal heterojunction and heterojunction wafer. c) EDS line scan profiles of the $MAPbCl_3/MAPbBr_3$ heterojunction. d) *I–V* curves of Au/$MAPbCl_3$-$MAPbBr_3$/Au heterojunction wafer under dark and 525 nm illumination conditions.

which lay a foundation for the industrial fabrication of perovskite-based devices.[23]

Even more, the transparent perovskite wafer manufacturing technique can also be extended to prepare double-layer and even multilayer perovskite heterojunction wafers. **Figure** 3a presents the photographs of our as-fabricated perovskite heterojunction wafers, including $MAPbCl_3/MAPbBr_3$, $MAPbCl_3$:Bi/$MAPbBr_3$, $MAPbCl_3$:Bi/$MAPbBr_3$/$MAPbBr_3$:Bi and $MAPbCl_3$:Bi/$MAPbCl_3$/$MAPbBr_3$/$MAPbBr_3$:Bi (The transparent perovskite wafer manufacturing technique is universal for different types of perovskite heterojunctions, taking Bi ion doping as an example). In Figure 3b, the cross-section SEM gives the detailed microstructures of transparent $MAPbCl_3/MAPbBr_3$ heterojunction wafers in comparison with the epitaxial single crystal heterojunction. The wafer layers exhibit uniform thickness distribution, and the heterojunction shows excellent uniformity along with compact interlayer connections and clear boundaries. The energy-dispersive spectroscopy (EDS) mapping analysis reveals a clear border between Chlorine (Cl) and bromine (Br) across different layers, indicating the distinct compositional characteristics of each layer, further corroborating the heterogeneous nature of the material. However, a halide ion diffusion length of 45 μm was also observed in the quantitative EDS line-scan analysis (Figure 3c), which can be attributed to halide ion diffusion. Even so, the diffusion region is also significantly smaller than that in the single-crystal heterojunction (59 μm). This result further confirms that our perovskite wafers can effectively suppress ion diffusion. The photoluminescence (PL) properties of the $MAPbCl_3/MAPbBr_3$ heterojunction wafers were studied. As shown in Figure S10 (Supporting Information), the heterojunction wafer revealed two well-resolved emission peaks corresponding to the constituent $MAPbCl_3$ and $MAPbBr_3$ phases. The absence of intermediate emission features between the characteristic $MAPbCl_3$ and $MAPbBr_3$ PL peaks indicates the formation of a built-in electric field at the heterointerface, which facilitates efficient transport of photogenerated charge carriers within the heterojunction architecture. The energy-band alignment at the heterojunction plays a decisive role in the separation and extraction of photogenerated charge carriers. Based on the ultraviolet photoelectron spectroscopy (UPS) (Figure S11a, Supporting Information) and absorption spectra (Figure S11b,c, Supporting Information), the valence band maximum (E_{VBM}), Fermi level (E_F), and conduction band minimum (E_{CBM}) of the wafers were calculated, as shown in Figure S11d. The E_F of the $MAPbCl_3$ wafer is close to the E_{CBM}, indicating its nature as an n-type semiconductor, whereas the E_F of the $MAPbBr_3$ wafer is near the E_{VBM}, suggesting its classification as a *p*-type semiconductor. With the band alignment of $MAPbCl_3$ and $MAPbBr_3$ in thermodynamic equilibrium, an internal electric field from *n*-type $MAPbCl_3$ to *p*-type $MAPbBr_3$ is formed, as shown in Figure S12, and the field significantly affected the efficient carrier separation. To further investigate the electron transport properties, the current density–voltage (*I–V*) curves of heterojunction wafer under dark and 525 nm illumination were measured (Figure 3d), which exhibited a typical diode effect, namely, conduction at positive bias and cutoff at negative bias,

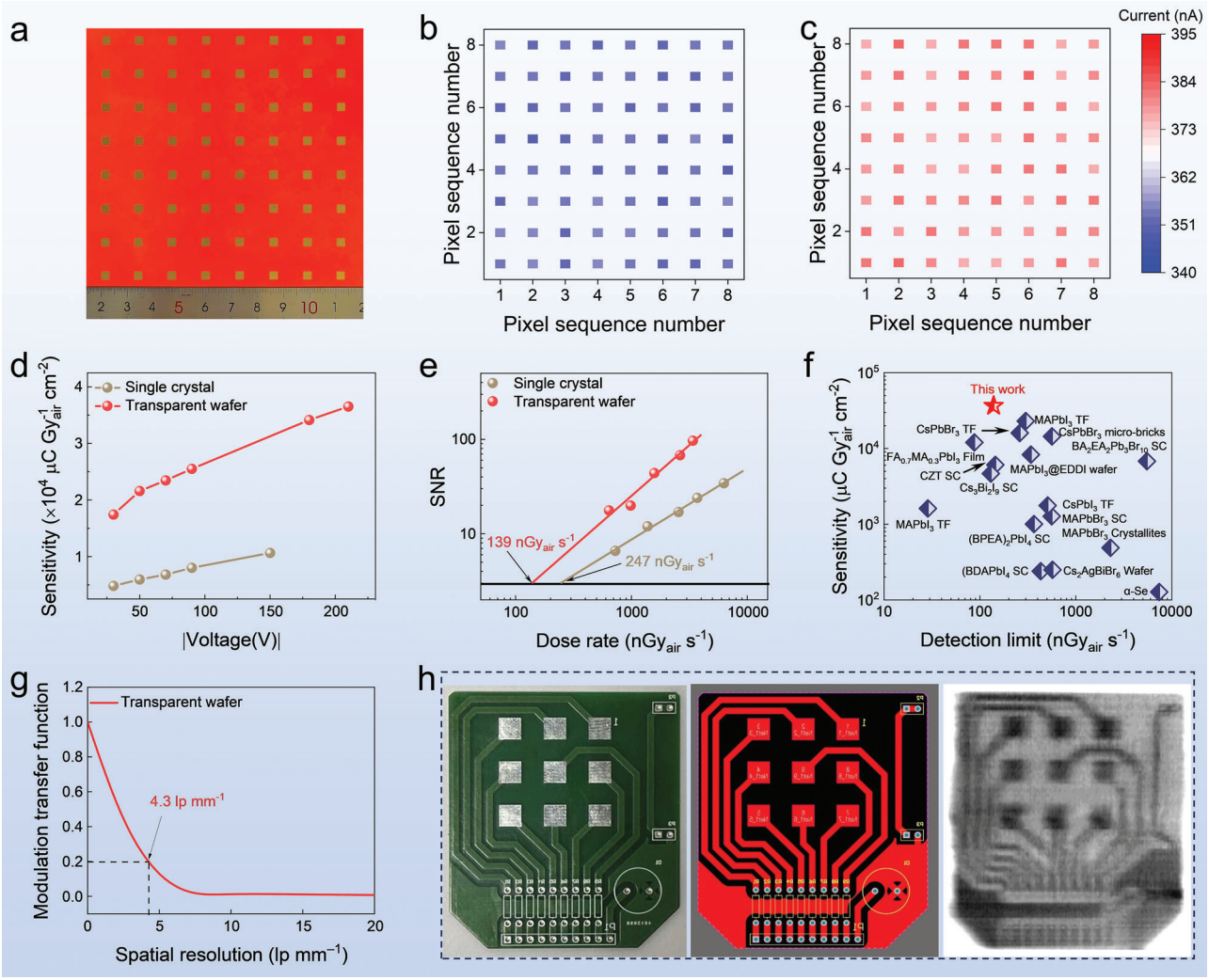

Figure 4. X-ray imaging based on the transparent perovskite heterojunction wafer. a) An optical image of an 8 × 8 pixels array fabricated from the transparent wafer, with a pixel size of 3 mm and a pitch size of 10 mm over a device area of 10 × 10 cm^2. The current uniformity of pixels (area of each pixel: 3 mm × 3 mm) as the regions of b) dark current and c) photocurrent. d) X-ray sensitivity. e) SNR of the pixels. f) The comparison of sensitivity and detection limit with previously reported perovskite X-ray detectors. g) The spatial resolution of the transparent wafer X-ray sensing array contains 256 × 256 pixels. h) Optical image, schematic diagram, and X-ray image of a printed circuit board (PCB) with an array of 256 × 256 pixels.

with distinct current values under different biases. In particular, under a negative bias, owing to the matching directions of the applied electric field and the built-in electric field in the space charge region, the energy-band barrier of the heterojunction was significantly increased, which effectively prevents electrons and holes from migrating through the space-charge region, and thus contributed to a decrease in the dark current.

To assess the potential for practical application, we employ our transparent perovskite wafer for constructing functional devices. As X-ray sensing sets stringent requirements on active material, we chose the X-ray sensing array on a transparent $MAPbCl_3$/MAPbBr heterojunction wafer. Figure S13 (Supporting Information) shows its attenuation efficiency for 40 keV X-ray photons. The $MAPbBr_3$ wafer exhibits strong X-ray attenuation due to its high absorption coefficient. As shown in **Figure 4a**, we first established an 8 × 8-pixel array was established on a heterojunction wafer with an area of 10 × 10 cm^2. To evaluate the uniformity of pixels, we measured the dark current and photocurrent of each pixel (under an X-ray dose rate of 20 $\mu Gy_{air}\ s^{-1}$) at a bias voltage of −30 V. As shown in Figure 4b,c, the standard deviation to average signal ratio was calculated to be 5.3% for dark current and 8.4% for photocurrent, respectively. Both are better than standard regulations.[14b] Figure 4d presents the sensitivity under various electric fields, which was derived from the slope of the photocurrent densities versus X-ray dose rates (Figures S14–S16, Supporting Information). As the working voltage increases (from −30 to −210 V), the sensitivity of our transparent wafer device rises from 1.74 × 10^4 to 3.65 × 10^4 $\mu CGyair^{-1}\ cm^{-2}$, which is ≈4 times higher than that of the single crystal device. Figure 4e shows the detection limit under a signal-to-noise ratio (SNR) of 3. Under the applied voltage of −30 V, the detection limit was estimated to be 139 $nGy_{air}\ s^{-1}$, which is better than that of the single crystal device (247 $nGy_{air}\ s^{-1}$). Notably, The obtained sensitivity is three orders of magnitude

higher than that of α-Se (20 μC Gy_{air}^{-1} cm^{-2}),[24] five times higher than that of the CZT detector (6069 μC Gy_{air}^{-1} cm^{-2})[8] and much higher than that of $MAPbI_3$ films (23 000 μC Gy_{air}^{-1} cm^{-2}),[25] $CsPbBr_3$ film (1450 μC Gy_{air}^{-1} cm^{-2})[26] and $Cs_2AgBiBr_6$ Wafer (250 μC Gy_{air}^{-1} cm^{-2})[14b] (Figure 4f; Table S5, Supporting Information). The detection limit is ≈38 times lower than the current medical diagnostic threshold (5.5 $\mu Gy_{air} s^{-1}$) and comparable to the reported representative single crystal detectors (Figure 4f; Table S5, Supporting Information).[27] Figure S17 (Supporting Information) shows faster rise and fall times (24.7 and 25.4 μs) in the pixel, enabling high-speed X-ray imaging. The response stability of the $MAPbCl_3/MAPbBr_3$ heterojunction wafer detector was measured under X-rays with a dose rate of 95 μGy_{air} s^{-1} and at a bias of −30 V for 3700 s, as shown in Figure S18a (Supporting Information). It can be seen that both the photocurrent and dark current of the detector remain stable without obvious degradation throughout the measurement period. The long-term stability of the heterojunction wafer in an air atmosphere is the key characterization for their practical applications. The response current of the wafer detector was calculated and remained at 97% of the initial value after 15 days (Figure S18b, Supporting Information). The excellent stability of the detector is attributed to the high crystalline quality and suppressed ion migration of the $MAPbCl_3/MAPbBr_3$ heterojunction wafer.

According to the established regulations, the artifacts and the ratio of the standard deviation to the mean signal in X-ray imaging should be less than 10%.[14b] Thus, we further fabricated a sensing array containing 256 × 256 pixels on a 10 × 10 cm^2 transparent wafer with a pixel pitch of 200 μm. By using the slanted-edge method,[22] the spatial resolution of the sensing array was calculated to be 4.3 lp mm^{-1} when the modulation transfer function of the detector was 0.2 (Figure 4g; Figure S19, Supporting Information). The object used for array imaging, as illustrated in Figure 4h and Figure S20 (Supporting Information), consists of a circuit board featuring diverse materials, including an epoxy resin substrate and copper circuit traces. During imaging, the X-ray dose rate was set to that of regular medical diagnostics (5.5 μGy s^{-1}). The images contain a clear and comprehensive morphology and internal structure of the circuit board. Additionally, discrimination among materials of different compositions has been achieved. It confirms that our sensing array based on a transparent wafer is suitable for high-quality X-ray imaging.

3. Conclusion

In summary, this work presents a breakthrough in scalable manufacturing of wafer-scale lead halide perovskite wafers, achieving optoelectronic properties approaching those of single crystals with the ceramic manufacturing technique. By precisely controlling temperature, pressure, and duration during fabrication, we successfully produced 6-inch transparent $MAPbBr_3$ wafers with exceptional optical transparency (≈68% in 700–1100 nm), high carrier mobility (hole: 99 cm^2 V^{-1} s^{-1}; electron: 180 cm^2 V^{-1} s^{-1}), and ultralow trap density (1.0 × 10^{10} cm^{-3}), rivaling the performance of $MAPbBr_3$ single crystals. The technique demonstrates universality across diverse perovskite compositions (A/B/X-site variations) and multilayer heterojunctions. Leveraging these advances, we fabricated a 10 × 10 cm^2 X-ray sensing array with 256 × 256 pixels, achieving ultrahigh sensitivity (36532 μC Gy_{air}^{-1} cm^{-2}) and ultralow detection limit (139 nGy_{air} s^{-1}), surpassing both single-crystal detectors and commercial counterparts. We believe this work bridges the critical gap between lab-scale perovskite research and industrial manufacturing, offering a universal platform for wafer-scale integration of perovskite devices with silicon-compatible processes.

4. Experimental Section

Preparation of the $MAPbBr_3$ Perovskite Wafers: Perovskite microcrystals were synthesized using the inverse temperature crystallization method, followed by drying and grinding into finer powder particles.[28] The specific procedure entailed the transfer of a 15 mL solution of N,N-dimethylformamide (DMF) into a beaker using a pipette. Subsequently, 3.54 g of methylammonium bromide (MABr) powder was added to the beaker and stirred on a magnetic stirrer until the salt was completely dissolved. Then, 11.12 g of lead bromide ($PbBr_2$) powder was added and stirred until the solution became clear and transparent. The solution was then filtered using a 22 μm organic filter to prepare a precursor solution with an MABr concentration of 1 mol L^{-1}. The precursor solution was placed on a stirring heater and stirred for 3 h at 80 °C, leading to the precipitation of $MAPbBr_3$ microcrystals as the solubility decreased. The microcrystals were subsequently dried in a vacuum dryer at 60 °C for 12 h, followed by grinding into smaller particles (≈50 μm) using an agate mortar and pestle to obtain the $MAPbBr_3$ perovskite powder necessary for hot pressing. The powder was then loaded into a hot-pressing mold, and the corresponding temperature, pressure, and time settings were adjusted before applying pressure once the set temperature was reached. Following hot pressing, the equipment was allowed to cool down to 50 °C, and the hot-pressed wafers were subsequently removed from the mold.

Preparation of Perovskite Heterostructures Wafers: The Perovskite heterojunction wafers were fabricated via a layer-by-layer hot-press assembly. The $MAPbBr_3$ microcrystalline precursor powders were sequentially loaded into a custom hot-press mold. An initial pressure of ≈10 MPa was applied after the deposition of each precursor layer to ensure uniform thickness, complete coverage, and homogeneous powder distribution. The subsequent layer (the $MAPbCl_3$ microcrystalline precursor powders) was added only after the preceding layer ($MAPbBr_3$) stabilized. After complete assembly, set the appropriate temperature and time, and immediately apply pressure to the hot-press mold once the set temperature was reached. Following hot pressing, the equipment was allowed to cool down to 50 °C, and the hot-pressed heterojunction wafers were subsequently removed from the mold. For multilayer perovskite heterostructures, an initial pressure of ≈10 MPa was applied after the deposition of each precursor layer to ensure uniform thickness, complete coverage, and homogeneous powder distribution. Subsequent layers were added only after the preceding layer stabilized. After complete assembly, the aforementioned hot pressing process was repeated, producing monolithic perovskite heterocrystalline wafers. The wafer dimensions and thickness were controlled by adjusting the mold size and the mass of precursor powder.

Fabrication of the Detectors: A vertical Au-$MAPbBr_3$-Au photodetector structure was fabricated through a process involving the application of a rigid masking film on both the top and bottom surfaces of the $MAPbBr_3$ wafer, followed by the deposition of square Au electrodes (50 nm thick, with an area of 2.5 mm × 3 mm) within a vacuum chamber.

In the case of the sensing array, it was fabricated on the transparent perovskite heterojunction wafer with a circular area measuring 15 cm in diameter. The top and bottom surfaces of the polycrystalline wafer were then affixed to PCB boards featuring horizontally and vertically arranged electrodes, utilizing a specially formulated crystal adhesive developed within the research group. The overlapping regions of the electrodes served as pixel points (size of 200 μm × 200 μm). The preparation of the crystal adhesive entailed a precise procedure, involving the addition of ethyl cellulose powder (1 g each, added thrice) into 9 mL of turpentine alcohol. The resulting mixture was then stirred and heated on a magnetic stirrer

heating plate at 90 °C for 2 h. Following this, 10 mL of $MAPbBr_3$ precursor solution was added to a beaker and vigorously stirred with a glass rod to promote fusion, after which the solution was further stirred and heated for 1 h to yield an orange viscous crystal adhesive.

Characterizations: Transmission spectra of all samples were acquired using a Cary 5000 UV–vis–NIR spectrophotometer (Agilent Technologies). The steady-state PL spectra were collected with an FS5 spectrofluorometer (Edinburgh Instruments, UK). The TRPL measurements were performed using a picosecond pulsed diode laser for excitation and a time-correlated single-photon counting detector for signal collection. The X-ray diffraction patterns were tested using a Rigaku SmartLab SE X-ray diffractometer and Cu Ka radiation (1.5406 Å). SEM images and EDS were investigated using Field-Emission scanning electron microscopy (Quanta 200 FEI). The noise current was extracted from the dark current recorded by an Agilent oscilloscope (7.5G) with a current amplifier. The electrical characteristics, represented by *I–V* and *I–T* curves, were measured using a Keithley 2400 parameter analyzer. To determine the rise time and fall time, the frequency of the light source (525 nm LED) was controlled utilizing an Agilent 33500B function generator. X-ray was generated by an Amptek Mini-X2 and the dose rate was calibrated using a 10×6-180 dosimeter (Radcal, USA). For X-ray imaging purposes, the detector connected to the PCB board was interfaced with the array imaging system developed by the research team via a ribbon cable, facilitating amplification and readout of pixel charges.

Supporting Information

Supporting Information is available from the Wiley Online Library or from the author.

Acknowledgements

This work at SEU was financially supported by the National Key Research and Development Program of China (2022YFE0139100), the NSFC (Nos. T2322003, 52172146, 62175028), the International cooperative research project of Jiangsu province (BZ2022008), and the Fundamental Research Funds for the Central Universities (No. 2242024K40017).

Conflict of Interest

The authors declare no conflict of interest.

Data Availability Statement

The data that support the findings of this study are available in the supplementary material of this article.

Keywords

ceramic, heterojunction, perovskites wafer, six-inch, X-ray array

Received: March 17, 2025
Revised: April 24, 2025
Published online:

[1] K. Choi, M. J. Jeong, S. Lee, G. Alosaimi, J. Seidel, J. S. Yun, J. H. Noh, *ACS Appl. Mater. Interfaces* **2022**, *14*, 24341.

[2] a) M. Y. Han, Y. R. Xiao, C. Zhou, Z. J. Xiao, W. Y. Tan, G. W. Yao, X. X. Wu, R. Z. Zhuang, S. M. Deng, Q. Hu, Y. X. Yang, Z. H. Tang, X. S. Zhou, H. B. Lin, H. L. Liang, S. H. Lin, Z. X. Mei, C. L. Wang, Q. Chen, W. Zhang, Y. Jiang, *Adv. Funct. Mater.* **2023**, *33*, 2303376; b) H. T. Wei, Y. J. Fang, P. Mulligan, W. Chuirazzi, H. H. Fang, C. C. Wang, B. R. Ecker, Y. L. Gao, M. A. Loi, L. Cao, J. S. Huang, *Nat. Photonics* **2016**, *10*, 333; c) D. Liu, Y. Zheng, X. Y. Sui, X. F. Wu, C. Zou, Y. Peng, X. Liu, M. Lin, Z. Wei, H. Zhou, Y.-F. Yao, S. Dai, H. Yuan, H. G. Yang, S. Yang, Y. Hou, *Nat. Commun.* **2024**, *15*, 2390.

[3] a) H. Zhang, Z. Yang, M. Zhou, L. Zhao, T. Jiang, H. Yang, X. Yu, J. Qiu, Y. Yang, X. Xu, *Adv. Mater.* **2021**, *33*, 2102529; b) B. Wang, J. Peng, X. Yang, W. Cai, H. Xiao, S. Zhao, Q. Lin, Z. Zang, *Laser Photonics Rev.* **2022**, *16*, 2100736.

[4] W. Chen, Z. Huang, H. Yao, Y. Liu, Y. Zhang, Z. Li, H. Zhou, P. Xiao, T. Chen, H. Sun, J. Huang, Z. Xiao, *Nat. Photonics* **2023**, *17*, 401.

[5] a) Q. Han, J. Wang, S. Tian, S. Hu, X. Wu, R. Bai, H. Zhao, D. W. Zhang, Q. Sun, L. Ji, *Nat. Commun.* **2024**, *15*, 1536; b) Z. Xu, X. Han, W. Wu, F. Li, R. Wang, H. Lu, Q. Lu, B. Ge, N. Cheng, X. Li, G. Yao, H. Hong, K. Liu, C. Pan, *Light, Sci. Appl.* **2023**, *12*, 67.

[6] Z. H. Guan, L. L. Fu, Z. Y. Wei, N. Y. Shan, H. Li, Y. Fang, Y. Zhao, Z. P. Huang, M. G. Humphrey, C. Zhang, *Mater. Today Phys.* **2023**, *35*, 101135.

[7] a) T. Wang, G. Lian, L. Huang, F. Zhu, D. Cui, Q. Wang, Q. Meng, C.-P. Wong, *ACS Appl. Mater. Interfaces* **2020**, *12*, 38314; b) T. Wang, G. Lian, L. Huang, F. Zhu, D. Cui, Q. Wang, Q. Meng, H. Jiang, G. Zhou, C.-P. Wong, *Nano Energy* **2019**, *64*, 103914.

[8] P. Zhang, Y. Hua, Y. Xu, Q. Sun, X. Li, F. Cui, L. Liu, Y. Bi, G. Zhang, X. Tao, *Adv. Mater.* **2022**, *34*, 2106562.

[9] M. Yang, Z. Nie, X. Li, R. Wang, Y. Zhao, H. Wang, *J. Mater. Chem. C* **2023**, *11*, 5908.

[10] a) L. Zhao, Y. Zhou, Z. F. Shi, Z. Y. Ni, M. R. Wang, Y. Liu, J. S. Huang, *Nat. Photonics* **2023**, *17*, 315; b) L. Ma, Z. G. Yan, X. Y. Zhou, Y. Q. Pi, Y. P. Du, J. Huang, K. W. Wang, K. Wu, C. Q. Zhuang, X. D. Han, *Nat. Commun.* **2021**, *12*, 2023; c) F. Yao, J. Peng, R. Li, W. Li, P. Gui, B. Li, C. Liu, C. Tao, Q. Lin, G. Fang, *Nat. Commun.* **2020**, *11*, 1194.

[11] K. Sakhatskyi, B. Turedi, G. J. Matt, E. R. Wu, A. Sakhatska, V. Bartosh, M. N. Lintangpradipto, R. Naphade, I. Shorubalko, O. F. Mohammed, S. Yakunin, O. M. Bakr, M. V. Kovalenko, *Nat. Photonics* **2023**, *17*, 510.

[12] a) S. Deumel, A. van Breemen, G. Gelinck, B. Peeters, J. Maas, R. Verbeek, S. Shanmugam, H. Akkerman, E. Meulenkamp, J. E. Huerdler, M. Acharya, M. Garcia-Batlle, O. Almora, A. Guerrero, G. Garcia-Belmonte, W. Heiss, O. Schmidt, S. F. Tedde, *Nat. Electron.* **2021**, *4*, 681; b) W.-G. Li, X.-D. Wang, Y.-H. Huang, D.-B. Kuang, *Adv. Mater.* **2023**, *35*, 2210878.

[13] L. Zhang, C. M. Liu, L. R. Wang, C. L. Liu, K. Wang, B. Zou, *Angew. Chem., Int. Ed.* **2018**, *57*, 11213.

[14] a) W. Li, L. Liu, M. Tan, Y. He, C. Guo, H. Zhang, H. Wei, B. Yang, *Adv. Funct. Mater.* **2021**, *31*, 2107843; b) B. Yang, W. Pan, H. Wu, G. Niu, J. H. Yuan, K. H. Xue, L. Yin, X. Du, X. S. Miao, X. Yang, Q. Xie, J. Tang, *Nat. Commun.* **2019**, *10*, 1989.

[15] a) M. Hu, S. Jia, Y. Liu, J. Cui, Y. Zhang, H. Su, S. Cao, L. Mo, D. Chu, G. Zhao, K. Zhao, Z. Yang, S. F. Liu, *ACS Appl. Mater. Interfaces* **2020**, *12*, 16592; b) S. S. Jia, Y. R. Xiao, M. X. Hu, X. L. He, N. Bu, N. Li, Y. C. Liu, Y. X. Zhang, J. Cui, X. D. Ren, K. Zhao, M. Liu, S. B. Wang, N. Y. Yuan, J. N. Ding, Z. Yang, S. Z. Liu, *Adv. Mater. Technol.* **2021**, *7*, 6; c) Y. R. Xiao, S. S. Jia, N. Bu, N. Li, Y. C. Liu, M. Liu, Z. Yang, S. Z. Liu, *J. Mater. Chem. A.* **2021**, *9*, 25603; d) S. Y. Dong, D. Y. Xin, M. Zhang, S. J. Tie, B. Cai, Q. S. Ma, X. J. Zheng, *J. Mater. Chem. C.* **2022**, *10*, 6236; e) X. J. Zheng, W. Zhao, P. Wang, H. R. Tan, M. I. Saidaminov, S. J. Tie, L. G. Chen, Y. F. Peng, J. D. Long, W. H. Zhang, *J. Energy Chem.* **2020**, *49*, 299; f) S. Tie, W. Zhao, D. Xin, M. Zhang, J. Long, Q. Chen, X. Zheng, J. Zhu, W.-H. Zhang, *Adv. Mater.* **2020**, *32*, 2001981.

[16] a) X. Zhang, T. Zhu, C. Ji, Y. Yao, J. Luo, *J. Am. Chem. Soc.* **2021**, *143*, 20802; b) V. Murgulov, C. Schweinle, M. Daub, H. Hillebrecht, M. Fiederle, V. Dedic, J. Franc, *Crystals* **2021**, *11*, 1208.

[17] a) W. Wu, J. Zhang, C. Liu, J. Zhang, H. Lai, Z. Hu, H. Zhou, *Adv. Sci.* **2024**, *11*, 2410303; b) W. Ming, Z. Jiang, G. Luo, Y. Xu, W. He, Z. Xie,

D. Shen, L. Li, *Nanomaterials* **2022**, *12*, 1491; c) I. Milisavljevic, M. J. Pitcher, J. Li, S. Chenu, M. Allix, Y. Wu, *Int. Mater. Rev.* **2022**, *68*, 648.

[18] a) H. Furuse, T. Okabe, H. Shirato, D. Kato, N. Horiuchi, K. Morita, B.-N. Kim, *Opt. Mater. Express* **2021**, *11*, 1756; b) A. Krell, P. Blank, H. Ma, T. Hutzler, M. P. B. van Bruggen, R. Apetz, *J. Am. Ceram. Soc.* **2004**, *86*, 12; c) S. Hříbalová, W. Pabst, *J. Eur. Ceram. Soc.* **2021**, *41*, 2169; d) R. Johnson, P. Biswas, P. Ramavath, R. S. Kumar, G. Padmanabham, *Trans. Indian Ceram. Soc.* **2012**, *71*, 73; e) A. Krell, T. Hutzler, J. Klimke, *J. Eur. Ceram. Soc.* **2009**, *29*, 207; f) S. F. Wang, J. Zhang, D. W. Luo, F. Gu, D. Y. Tang, Z. L. Dong, G. E. B. Tan, W. X. Que, T. S. Zhang, S. Li, L. B. Kong, *Prog. Solid State Chem.* **2013**, *41*, 20.

[19] a) Z. Tang, Z. Huang, W. Han, J. Qi, N. Ma, Y. Zhang, T. Lu, *Scr. Mater.* **2020**, *178*, 90; b) B. Peng, Q. Shi, W. Huang, S. Wang, J. Qi, T. Lu, *Ceram. Int.* **2018**, *44*, 13674; c) L. Zhang, J. Feng, W. Pan, *Ceram. Int.* **2015**, *41*, 8755; d) Z. Xiao, S. Yu, Y. Li, S. Ruan, L. B. Kong, Q. Huang, Z. Huang, K. Zhou, H. Su, Z. Yao, W. Que, Y. Liu, T. Zhang, J. Wang, P. Liu, D. Shen, M. Allix, J. Zhang, D. Tang, *Mater Sci Eng R: Rep.* **2020**, *139*, 100518.

[20] P. J. Sellin, A. W. Davies, A. Lohstroh, M. E. Ozsan, J. Parkin, *IEEE Trans. Nucl. Sci.* **2005**, *52*, 3074.

[21] Y. Shao, Y. Fang, T. Li, Q. Wang, Q. Dong, Y. Deng, Y. Yuan, H. Wei, M. Wang, A. Gruverman, J. Shield, J. Huang, *Energy Environ. Sci.* **2016**, *9*, 1752.

[22] J. Yu, Y. Luo, N. Tian, Y. Liu, Z. Yang, J. Pi, L. Li, R. Zheng, C. Wang, S. Liu, *Adv. Mater.* **2024**, *37*, 2413709.

[23] K. Bartosiewicz, A. Szysiak, R. Tomala, P. Golebiewski, H. Weglarz, V. Nagirnyi, M. Kirm, I. Romet, M. Buryi, V. Jary, R. Kucerkova, M. Wzorek, R. Buczynski, *Phys. Rev. Appl.* **2023**, *20*, 014047.

[24] H. Wu, Y. Ge, G. Niu, J. Tang, *Matter* **2021**, *4*, 144.

[25] Z. Y. Zhu, B. Zhao, R. He, H. W. Chen, S. Gao, Y. He, Y. L. Li, *ACS Appl. Mater. Interfaces* **2024**, *16*, 38799.

[26] G. J. Matt, I. Levchuk, J. Knuettel, J. Dallmann, A. Osvet, M. Sytnyk, X. Tang, J. Elia, R. Hock, W. Heiss, C. J. Brabec, *Adv. Mater. Interfaces* **2020**, *7*, 1901575.

[27] a) W. Li, H. Li, J. Song, C. Guo, H. Zhang, H. Wei, B. Yang, *Sci. Bull.* **2021**, *66*, 2199; b) H. Q. Zhong, S. H. You, J. B. Wu, Z. K. Zhu, P. P. Yu, H. Li, Z. Y. Wu, Y. Li, Q. W. Guan, H. L. Dai, C. Qu, J. H. Wang, S. Chen, C. M. Ji, J. H. Luo, *JACS Au* **2024**, *4*, 2393.

[28] Z. Hong, D. Tan, R. A. John, Y. K. E. Tay, Y. K. T. Ho, X. Zhao, T. C. Sum, N. Mathews, F. Garcia, H. S. Soo, *Iscience* **2019**, *16*, 312.